On the noise estimation in Super Dual Auroral Radar Network data

P. V. Ponomarenko[1], E. C. Bland[2], K. McWilliams[1], and N. Nishitani[3]

[1]Institute of Space and Atmospheric Studies, University of Saskatchewan, Saskatoon, SK, Canada

[2]Department of Arctic Geophysics, University Centre in Svalbard, Norway

[3]Institute for Space-Earth Environmental Research, Nagoya University, Japan

Abstract

The Super Dual Auroral Radar Network (SuperDARN) currently consists of more than thirty high-frequency (HF, 3–30 MHz) radars covering mid-latitude to polar regions in both hemispheres. Their major task is to map ionospheric plasma circulation which provides information about the interactions between the solar wind and the near-Earth's space plasma environment. One of the major factors defining radar data quality is the signal-to-noise ratio (SNR), which requires an accurate characterisation of the HF noise. The standard SuperDARN data analysis software uses the SNR as part of a set of empirical procedures designed to remove low-quality data from further analysis. In this study we found that the currently used empirical algorithm systematically underestimates the noise level by up to 40%. Based on comparison of theoretical and observational noise statistics, we resolve this issue by designing and validating a procedure for accurate background noise level estimation. We then propose a simple SNR threshold to replace the existing criteria for excluding low-quality data. In addition, we show that several aspects of the radar operational regime design, as well as short-lived anthropogenic radio interference, can adversely affect the quality of the noise estimates at selected radar sites, and we propose ways to mitigate these problems.

1 Introduction

The Super Dual Auroral Radar Network (SuperDARN) is a global network of more than thirty high-frequency (HF) radars operating in 8–20 MHz frequency band and designed for studying high-latitude ionospheric plasma circulation in the northern and southern hemispheres (Greenwald et al., 1995). The radars detect backscatter from decameter-scale electron density structures, which are used as tracers of the $E \times B$ ionospheric plasma drifts at the E- and F-region heights. The radars also routinely detect ground scatter echoes from the Earth's surface illuminated by the radar signals refracted from the ionosphere (André et al., 1998), and backscatter from meteor plasma trails at ∼90–100 km altitude (Hall et al., 1997). These three types of radar echoes provide important information about physical processes in the upper atmosphere that are driven by both solar activity and atmospheric dynamics, including the spatio-temporal structure of global plasma circulation at high latitudes, substorms, magnetohydrodynamic waves, and gravity waves (Chisham et al., 2007; Nishitani et al., 2019, and references therein).

As with any scientific instrument, SuperDARN data are affected by noise, and these effects need to be accurately quantified in order to evaluate the data quality and to obtain accurate estimates of the measurement errors. In the standard SuperDARN data analysis software, the *Radar Software Toolkit* (SuperDARN Data Analysis Working Group, 2021), a package called FITACF performs these tasks in two stages consisting of (i) data pre-selection and (ii) error calculation. At the pre-selection stage, the package removes from further analysis the records which do not satisfy a set of empirical criteria for physically meaningful data. Importantly, several pre-selection procedures utilize a calculated estimate of the noise level. At the following stage, the measurement errors are estimated for the data that passed the pre-selection. Furthermore, the noise estimate is also used to determine the signal-to-noise ratio (SNR), which is commonly used as a data quality indicator.

As the thermal noise level in the radar's internal electronic circuitry is normally insignificant compared to that generated by the external sources, HF radio noise represents one of the main factors restricting the quality of the SuperDARN data products. At SuperDARN operating frequencies, radio noise arises from both natural and anthropogenic sources (ITU-R P.372-8, 2019). The dominant natural noise source is atmospheric noise, which is produced by lightning activity at mid-to-low geographic latitudes and propagates around the planet via consecutive 'reflections' from the ionosphere and the ground surface. The atmospheric noise exhibits diurnal and seasonal variations controlled by the ionospheric propagation conditions and the global distribution of lightning activity, and these variations can be observed using SuperDARN radars (Ponomarenko et al., 2016; Bland et al., 2018). Anthropogenic noise in the SuperDARN frequency range includes signals from other radio installations as well as radio emissions generated by nearby electronic and electrical equipment. Anthropogenic noise is therefore highly specific to radar site location, and it may represent the dominant noise source for SuperDARN radars located in populated areas.

While atmospheric HF noise has a detrimental effect on the quality of the received backscatter, it also contains useful information about ionospheric conditions. For example, there has been recent development in utilizing background noise measurements from SuperDARN radars to monitor ionospheric radiowave attenuation triggered by space weather events (Bland et al., 2018, 2019; Berngardt et al., 2019; Chakraborty et al., 2019; Berngardt, 2020). To provide accurate estimates of the SuperDARN data quality and to sup-

port scientific applications of the SuperDARN noise measurements, it is important to examine in detail the method for estimating the noise level so that we can assess its reliability. In this work we identify both network-wide and site-specific factors affecting the statistical validity of the noise estimation for SuperDARN data. Firstly, we review in detail how the noise level estimates are determined in FITACF, and show that the standard technique systematically underestimates the noise level by sampling only the low-power tail of the noise probability density function (PDF). To mitigate this problem, we propose a procedure that compensates for this systematic error. We then propose a simple and efficient data pre-selection procedure based on a single SNR threshold that can potentially replace the current set of the poorly-justified empirical selection criteria. Finally, we show that several features of the radar operation regime design, as well as short-lived anthropogenic radio interference, can introduce significant errors into the noise level estimates for particular radars, and we discuss ways to mitigate their impacts.

2 SuperDARN design and operation

SuperDARN comprises frequency-agile phased-array radars that operate in the 8–20 MHz frequency range. Each radar is equipped with a linear array of sixteen log-periodic or twin-terminated folded dipole antennas, which are phased electronically to produce a main lobe that is relatively narrow in azimuth ($3.5-4^\circ$ at 50% power). For most of the radars, the main lobe is consecutively steered through 16 fixed azimuthal directions (beams) separated by 3.24°, producing a total azimuthal field of view (FoV) of about 52°. Some newer radars operate with up to 24 beams and thus have broader FoVs. A map showing the fields of view of all SuperDARN radars is available in Nishitani et al. (2019, Fig. 1). Most SuperDARN radars are also equipped with a passive auxiliary interferometer antenna array consisting of only four elements, positioned about 100 m in front of or behind the main 16-element array. The phase offset between the signals received by the main and interferometer arrays is used for measuring the vertical angle of arrival of the received signals (Milan et al., 1997; Shepherd, 2017; Chisham et al., 2021).

In the standard operational mode, the radars sample along each beam direction in 45-km steps in group range starting from 180 km to about 3500–4000 km, forming 70–110 range cells (range gates) along the beam. To achieve both the range span and data sampling rate (maximum Doppler shift) required for mapping ionospheric plasma circulation, the radars transmit a sequence of seven or eight unevenly-spaced pulses to gen-

erate a continuous series of evenly-spaced time lags between 0 and 35-40 ms to form a complex-valued autocovariance function (ACF) for each range gate (Greenwald et al., 1985; Villain et al., 1996; Ponomarenko & Waters, 2006; Berngardt et al., 2015). To reduce the magnitude of statistical fluctuations, the ACFs are averaged over a period of either $\simeq$3.5 or $\simeq$7 s per beam direction, so a full scan of the entire FoV is completed within either 1 or 2 minutes. Furthermore, crosscovariance functions (XCFs) between the main and interferometer arrays are calculated in the same way and stored in the same format. While these data can be processed using a number of techniques developed over the last three decades (e.g. Barthes et al., 1998; Greenwald et al., 2008; Ponomarenko et al., 2008; Ribeiro et al., 2013; Reimer et al., 2018), in this study we consider only the standard analysis package, FITACF (e.g., see Appendix in Ponomarenko & Waters, 2006).

The most important data product for this study is the ACF power p at zero time lag conventionally referred to as the *lag zero power*. In panel (a) of Figure 1 we show a typical example of lag zero power measurements from beam 7 of the Inuvik (INV) SuperDARN radar, plotted as a function of time and range gate. The power measurements have arbitrary units (a.u.) originating from the radar's analogue-to-digital (A/D) converter. The color scale is saturated at the upper end in order to emphasize the detail in the lower part of the power distribution near the actual noise level. Ionospheric and ground scatter echoes can be identified visually in this plot as continuous patches of high-power ($\sim 10^4 - 10^6$ a.u.) data spanning up to 15 range gates and lasting from several minutes to several hours. The ranges at which these echoes are observed depend on the ionospheric electron density distribution along the ray path and the presence of suitable scattering targets. In the absence of the backscatter component, ACFs characterise the noise. Range gates dominated by noise can be identified in Figure 1 as those with power below about 10^3 a.u.. FITACF uses these noise-dominated range gates for calculating the SNR (see Section 3 for details). Here we just want to mention that the SuperDARN radars receive a mixture of the noise and the backscatter powers, $p^{sig+noi}$, and in order to calculate SNR one needs first to subtract a noise power p^{noi} from the mixture to obtain the signal power estimate and only then to divide the result by the noise power:

$$\mathrm{SNR} = \frac{p^{sig+noi} - p^{noi}}{p^{noi}}. \tag{1}$$

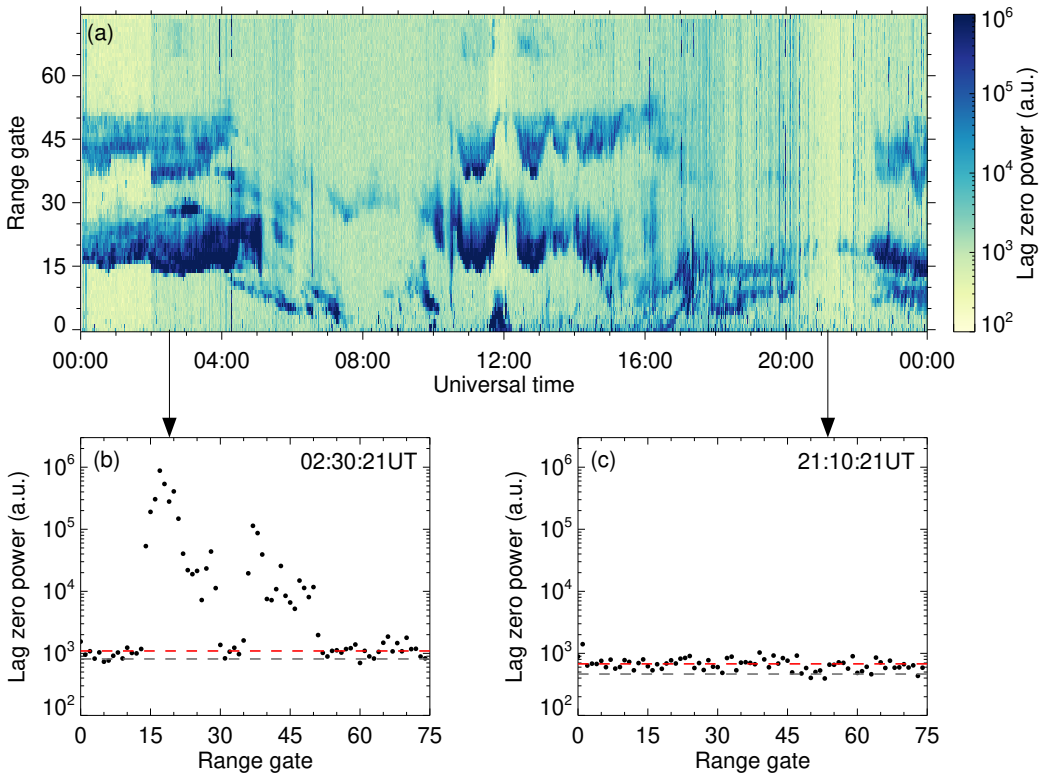

Figure 1. (a) Range-time-intensity plot showing the lag zero power measurements from beam 7 of the Inuvik (INV) SuperDARN radar on 4 April 2018. (b,c) Sample range-power dependence at two different integration intervals. The red dashed lines in the bottom panels show the noise level estimated from the full set of the noise-dominated range gates while the grey lines correspond to that estimated from the subset of ten lowest power values from these range gates (see text for details).

3 Noise level estimation

3.1 Noise level underestimate by standard SuperDARN method

The original FITACF package was developed in the late 1980s, and the implemented procedures were described in some detail in (Baker et al., 1988). The noise level determination was described as following; *"An initial noise level is determined from the average backscattered lag zero power from the 10 weakest ranges."*, but no further explanation or justification was provided. While FITACF has undergone significant modifications since its inception, our analysis of the most recent default version, FITACF2.5 (SuperDARN Data Analysis Working Group, 2021), revealed that indeed the mean noise level is currently estimated from the ten lowest values of the lag zero power observed during a given integration interval (beam-dwelling time). Based on the available information, we have deduced that this noise determination procedure was based on following assumptions:

- Noise is stationary: the noise power statistics do not change significantly within the integration time.
- Noise is uniform in group range: the noise power level is not related to the radar emission regime so that the mean and standard deviation are the same across all range gates.
- Lowest-power signals represent noise: the ten range gates with the lowest lag zero power values contain negligible contributions from the backscatter returns, i.e., their ACFs are fully defined by the noise.
- Unbiased power estimates: the mean lag zero power from these ten range gates represents an accurate estimate of the noise power.

While the first three assumptions seem to be reasonable, a detailed analysis reveals that the last assumption is problematic and leads to inaccurate noise estimates.

Panels (b) and (c) of Figure 1 show the lag zero power dependence on range gates obtained for two different sampling intervals. In panel (b) (02:30:21 UT), there are two power peaks reaching $\sim 10^5$–10^6 a.u. at gates 14–29 and 35–51, which are indicative of backscatter returns, while the remaining range gates are apparently dominated by the noise at $\sim 10^3$ a.u. The second example (21:10:21 UT) contains no backscatter returns and is characterised by noise power fluctuating around $\simeq 7-8 \cdot 10^2$ a.u.. The gray dashed

line in each plot shows the noise level determined from averaging the ten lowest lag zero power values. It is apparent from panel (c) that this estimate is noticeably biased towards lower values with respect to the mean calculated from all range gates, which is indicated by the red dashed line. A similar conclusion can also be derived from a close visual analysis of the data in panel (b). In this case, the mean noise power was calculated using the lag zero power values in all range gates except 14–29 and 35–51.

To clarify why the actual noise level is underestimated, let us first consider a case in which all N_{g} range gates contain noise samples only (i.e., like the data in Figure 1c). The correct way of calculating the mean value for a positively defined power p is by estimating a following integral between zero and infinity

$$\mu_p = \int_0^{\infty} pw\,(p)\,dp, \tag{2}$$

where $w\,(p)$ represents noise PDF. However, averaging over the ten lowest power values corresponds to the integration over the lower-power portion of the PDF,

$$\mu_{p_{10}} = \int_0^{p_{10}} pw\,(p)\,dp, \tag{3}$$

where p_{10} is a percentile value corresponding to the ten range gates with lowest lag zero power values. This lowering of the upper integration limit creates a bias towards lower values in the mean estimates, hence noise power underestimation occurs.

Now let us assume that some of the range gates also contain contributions from backscatter echoes. In this case the bias magnitude would decrease with decreasing the number of the noise-dominated range gates, N_g^{noi}, and becomes zero if there are only ten of those. However, in practice N_g^{noi} rarely goes below 30, as illustrated by Figure 1, so that the bias towards lower noise levels is practically always present in the data processed by FITACF2.5. A more detailed quantitative analysis of this effect is provided in section 3.4.

3.2 Observed noise statistics and proposed correction technique

To study the noise level underestimate by FITACF2.5 in more detail, we use data from a special receive-only mode that was run on the Saskatoon SuperDARN radar (SAS) from 15 April 2014 (12:00 UT) to 19 April 2014 (12:00 UT). For this mode, the transmitters did not emit any signal, but the receivers routinely sampled the antenna input to obtain noise-only ACFs. The receiver frequency alternated every minute between two different values, $\simeq$ 10 MHz and $\simeq$ 13 MHz, providing quasi-simultaneous noise mea-

surements at these two frequencies. A sample of the lag zero power measurements from this mode at the two different frequencies is shown in the top panels of Figure 2.

The previous studies show that the average noise level may vary significantly with time of day and frequency (e.g. Bland et al., 2018; Ponomarenko et al., 2016). This is evident in the top panels of Figure 1 and Figure 2, which show noticeable variations in the background color across all range gates. To make the daily data statistically compatible, we compensated for the noise power non-stationarity by normalizing the data from each $\simeq 3$ s integration interval by the mean power value for that interval so that the resulting mean is equal to one, $\bar{\mu} = 1$. This 'homogenisation' procedure allowed us to use all observational noise data as a single statistically stationary ensemble to closely examine the noise PDFs.

A conventional transmit-receive cycle for a single SuperDARN pulse sequence lasts for $\simeq 0.1$ s, so for a typical integration time of $\simeq$3 s, the number of averages, N_a, is close to 30. For example, the median number of averages for the data in Figure 2 was $N_a = 32$. To remove additional variations in PDF parameters caused by variations in N_a, we considered only the scans with exactly 32 averages, which accounts for about 90% of the analyzed receive-only data. We also excluded the data from the farthest gate #74 (note that the conventional range gate indexing begins from 0), which showed significantly higher p values representing a hardware artifact.

The lower panels of Figure 2 show histograms of these normalized noise power measurements, $\bar{p}$, for the April 2014 SAS dataset obtained at two frequency ranges, 10.5-10.8 MHz and 13.0-13.3 MHz. The black curves represent the data normalized by the mean noise power μ_p estimated from all 74 range gates (gates 0–73). The gray-shaded area on the left side under the black curve corresponds to the portion of data used by the conventional method (10 gates with lowest lag zero power values). It is immediately clear from equation (3) that the respective mean $\bar{\mu}_{10}$ cannot exceed the right margin of the gray shaded area $\bar{p}_{10} \simeq 0.77$. As a result, the conventional noise level estimate is significantly lower than the actual mean value (in this case $\bar{\mu}_{10} \simeq 0.6$ as compared to $\bar{\mu} = 1$). Therefore, normalizing the data by the conventional noise estimate $\mu_{p_{10}}$ (solid red curves in Figure 2) introduces a significant bias in the noise PDF location on the power axis when a majority of the noise data are shifted above the assumed mean noise level at $\bar{\mu} = 1$ (vertical dashed line).

An important observation that follows from examining these plots is that the actual noise distribution (black line) is essentially restricted to power values below the doubled mean, $2\mu_p$. For the data in Figure 2 the probability to observe noise with power in excess of $2\mu_p$ is less than 1%. From Equation 1, the power level of $2\mu_p$ corresponds to SNR = 1. This observation provides a simple and statistically transparent criterion for data pre-selection: we should analyze only the data for which

$$\mathrm{SNR} > 1. \tag{4}$$

There is an indication in the original FITACF code that this criterion may have been the initial intention of FITACF creators. However, at that time the noise underestimation was apparently unrecognized by the package authors and forced them to apply additional empirical criteria based on ACF power shape in order to remove the excessive amount of noise-dominated data (for more detail see, e.g., Appendix 3 in Ponomarenko & Waters, 2006). Indeed, the percentage of the noise data that exceeds the threshold (4),

$$P_{leak} = \frac{\int_{2\bar{\mu}}^{\infty} w\left(\bar{p}\right) d\bar{p}}{\int_{0}^{\infty} w\left(\bar{p}\right) d\bar{p}} \cdot 100\%, \tag{5}$$

is significantly higher for the conventional FITACF2.5 method (solid red curves in Figure 2) compared to the actual noise distribution (solid black curves). The respective portions of the noise PDFs are highlighted by the red shaded regions in Figure 2. For this dataset, P_{leak} at 10 MHz (13 MHz) increases from 0.4% (0.7%) for normalizing by μ_p to 4.5% (5.8%) for normalizing by $\mu_{p_{10}}$. In practical terms, instead of approximately one noise ACF misidentified as a valid backscatter ACF over three integration intervals, we get three to four such 'false positives' during each integration interval.

As the dataset used to analyze the noise PDF was limited to four days of data from a single radar, it is important to confirm that other radars observe similar noise characteristics. In Figure 3, the first and third rows show the range-time plots of the lag zero power measurements from beam 7 over a selection of mid-latitude (Fort Hays West, FHW, and Unwin, UNW), auroral (King Salmon, KSR, and Saskatoon, SAS) and polar cap (Clyde River, CLY, and McMurdo, MCM) SuperDARN radars in both hemispheres. The black boxes represent the time periods with no visually discernible contributions from ionospheric or ground scatter. The second and fourth rows show respective normalized statistical distributions calculated in the same way as those shown in Figure 2. All distri-

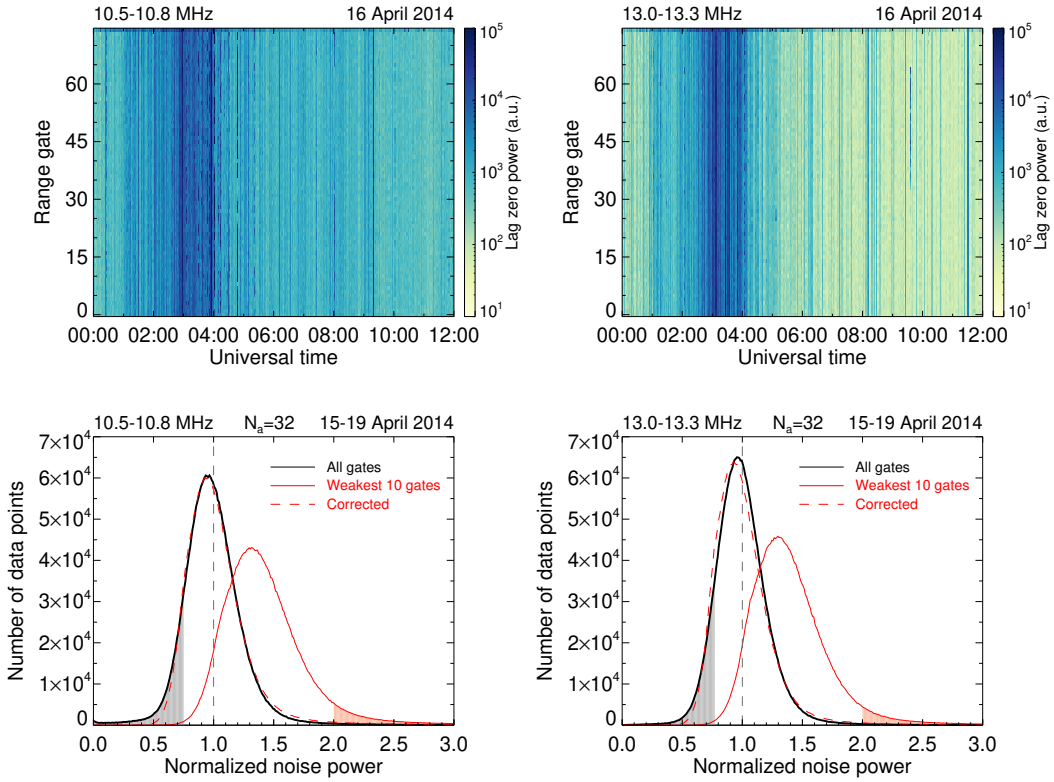

Figure 2. (Top panels) Sample lag zero power measurements from beam 7 of the Saskatoon (SAS) radar at 10.5–10.8 MHz and 13.0–13.3 MHz during a receive-only experimental mode. The time period shown is 16 April 2014, 00:00–12:00 UT. (Bottom panels) Noise power histograms at 10.5–10.8 MHz and 13.0–13.3 MHz for all beams of the SAS radar during the same receive-only experiment for the period 15–19 April 2014. The black curves show the noise power for each scan normalized by the mean calculated using power from all range gates, and the solid red curves show the data normalized by the mean of the ten lowest power values in each integration period (FITACF2.5 method). The gray shaded area represents the portion of the data used for estimating the mean noise level in the conventional software. The red shaded area represents the portion of the noise data that exceed the SNR=1 (p=2μ_p) threshold. The red dashed curves show the noise distribution from the FITACF2.5 method with a correction factor applied (see text for details).

bution graphs demonstrate a remarkable similarity to each other, suggesting the same statistical nature of the noise at all these locations.

From the above analysis it follows that to compensate for the noise level underestimation by the conventional FITACF algorithm, a correction factor

$$Q = \frac{\mu_p}{\mu_{p10}} \tag{6}$$

needs to be applied to the mean noise level estimated from the ten lowest lag zero power values μ_{p10}. This procedure requires information about the noise PDF parameters that is not readily obtainable in the presence of a backscatter component. To address this deficiency, a suitable PDF model adequately describing the statistical properties of the noise data is required. This issue is addressed in the following subsection.

3.3 Statistical noise model and comparison with observations

In SuperDARN data, complex ACFs are built from real and imaginary parts of the analytic signal

$$\tilde{s}(t) = s(t) + jH\left[s(t)\right], \tag{7}$$

where $s(t)$ is the received signal, $H\left[s(t)\right]$ its Hilbert transform, and j is the imaginary unit. In this case the mean lag zero power is calculated as

$$p = \sum_{i=1}^{N_a} \left(s_i^2 + \left(H\left[s_i\right]\right)^2 \right) \tag{8}$$

where s_i and $H\left[s_i\right]$ represent individual samples obtained over the integration period. As we are considering noise as a process arising from a large number of lightning strikes, according to the Central Limit Theorem $s(t)$ should represent a zero-centered Gaussian processes. Due to the fact that the Hilbert transform only shifts the phase of each frequency component by 90°, $s(t)$ and $H\left[s(t)\right]$ represent uncorrelated Gaussian processes with the same statistical parameters. Furthermore, consecutive samples in both processes are also uncorrelated as they are taken at intervals of approximately 100 ms, which are much larger than the noise autocorrelation time scale (not shown). As a result, equation (8) represents a sum of squares from $2N_a$ independent Gaussian processes characterized by zero mean and the same variance. In this case, the statistics for the noise power p are governed by a Chi-Square distribution $\chi^2_n(x)$ with $n = 2N_a$ degrees of freedom and argument $x = pn/\bar{\mu}$ (e.g. Bendat & Piersol, 2010). The χ^2 distribution is charac-

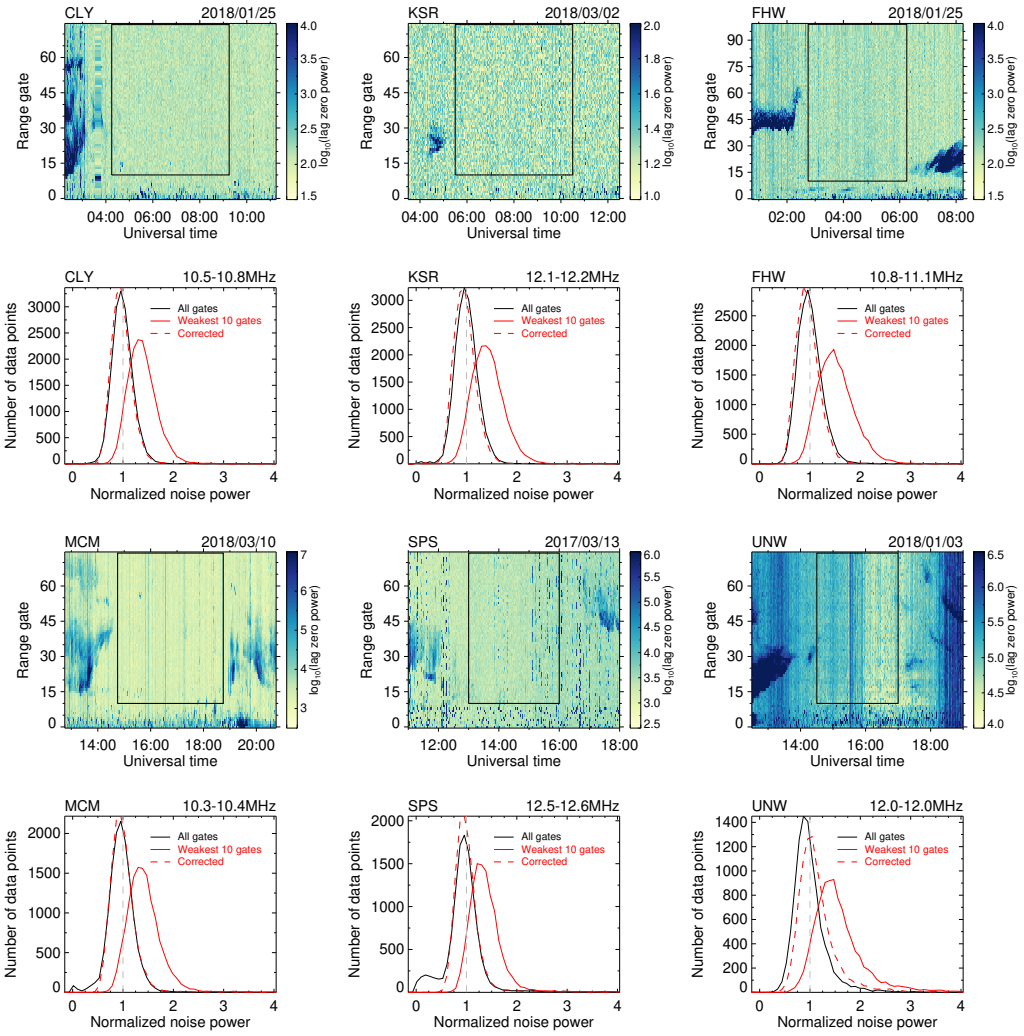

Figure 3. Sample lag zero power measurements and their corresponding noise power distributions from beam 7 for different SuperDARN radars. The analyzed noise datasets are indicated by the black rectangles in the range gate–UT panels. The histograms are in the same format as Figure 2. The red dashed lines show the data normalized by the standard FITACF2.5 method with the correction factor applied.

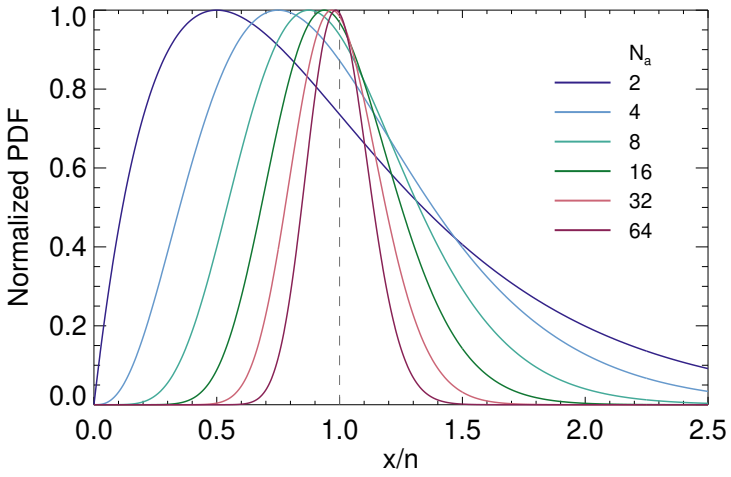

Figure 4. Normalized χ^2 distribution functions calculated for different number of averages N_a. Argument x is normalized by the number of degrees of freedom $n = 2N$a.

terised by the mean

$$\mu_{\chi^2} = n, \tag{9}$$

and the variance

$$\sigma^2_{\chi^2} = 2n. \tag{10}$$

As we analyze noise power normalized by the mean, p/μ_p, the argument should be divided by n giving following values for the mean

$$\bar{\mu} = \frac{\mu_{\chi^2}}{n} = 1, \tag{11}$$

and for the standard deviation

$$\bar{\sigma} = \frac{\sigma_{\chi^2}}{n} = \sqrt{\frac{2}{n}} = \frac{1}{\sqrt{N_a}} \tag{12}$$

In Figure 4 we show the theoretical PDFs $w(p/\mu_p)$ for different values of N_a. The PDF magnitudes have been normalized by their maximum values to allow the shapes to be readily compared. The resulting curves illustrate the well-known fact that with increasing the number of degrees of freedom, χ^2 asymptotically approaches the Gaussian shape.

In Figure 5 we compare the normalized noise power histogram for the 13 MHz data from Saskatoon (black line, same data as in the right panel of Figure 2) with the theoretical curves obtained for χ^2 (blue) and Gaussian (red) distributions calculated for $\bar{\mu} =$

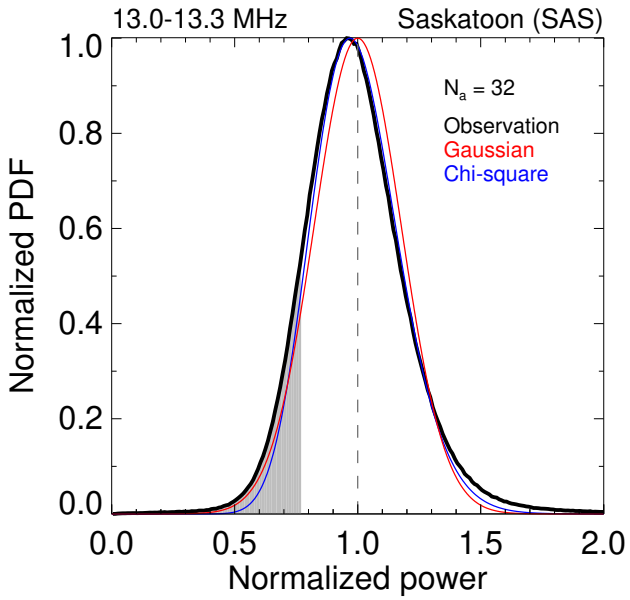

Figure 5. Normalized noise power histogram for the observed data (black) and probability density functions for χ^2 (blue) and Gaussian (red) models with $N_a = 32$ (see text for details). The measurements were taken during 15–19 April 2014.

1 and $N_a = 32$. Both theoretical distributions provide a reasonable match to the observations. Furthermore, the red dashed lines in Figures 2 and 3 represent the results of applying the correction factor (6) calculated from the Gaussian model to the noise estimated as a mean of the ten lowest lag zero power values (red solid lines). Visually these corrected distributions closely match the noise histograms estimated as a mean from all range gates. Importantly, very similar results were obtained for a selection of radar sites presented in Figure 3 which allows for the network-wide applicability of the described noise correction approach.

3.4 Validation of correction technique

So far we have considered only the case when the radar is not transmitting. For this special case, across all range gates the lag zero power contains only noise. When the radar is transmitting, the number of range gates containing only noise, N_g^{noi}, is lower than the total number of range gates as some of them contain a significant backscatter component. In this case the ten lowest lag zero power values represent a proportionally greater fraction of the total noise distribution thus producing larger values of p_{10} and,

consequently, a smaller correction factor Q. The problem here is that there is no reliable way to estimate N_g^{noi} automatically when the radar is transmitting.

A conservative way to address this issue is to apply the maximum possible value of the correction factor, Q_{all}, which occurs when we assume that all range gates contain only noise. While application of Q_{all} to the actual data containing backscatter leads to the noise level being overestimated, this overestimation is significantly smaller than the underestimation caused by averaging the ten lowest lag zero power values. To illustrate this, Figure 6 shows the dependence of P_{leak} (a) and the corrected sample mean $\mu_{10}Q_{all}$ (b) on N_g^{noi} based on Chi-Square (blue) and Gaussian (red) models. Variable values of N_g^{noi} were obtained using subsets of consecutive range gates in the SAS dataset from 15–19 April 2014, i.e., the first five, first 10, first 15, first 20, and so on. For reference we also show the uncorrected estimates from the ten range gates with lowest power values (solid black) and those obtained from all range gates (dashed black).

Both models produce remarkably similar results. As expected, the maximum difference between the corrected mean $\bar{\mu}_{10}Q$ and the mean estimated from all range gates $\bar{\mu}$ ($\simeq$25–30% in this case) is observed for $N_g^{noi} = 10$. In practice the proportion of range gates with backscatter echoes rarely exceeds 50%, i.e., $N_g^{noi} \gtrsim 35-40$. For this range of N_g^{noi}, P_{leak} decreases from 3–5% in the uncorrected data to below 1% while the mean noise estimate error is restricted to within $\pm$10–15% as compared to a positive 30–40% bias for the uncorrected data.

Based on the results presented in Figure 6, we have concluded that using the maximum value of the correction factor calculated from either the Chi-square or Gaussian model effectively mitigates the effects of the noise level underestimation by the conventional FITACF2.5 software. Based on this conclusion, we propose an improved two-stage noise level calculation procedure for SuperDARN data. At the first stage, the noise level is estimated from the mean of the ten lowest lag zero power values. At the second stage, a maximum value of the correction factor, Q_{all}, is calculated based on the Gaussian model with a unit mean and standard deviation of $1/\sqrt{N_a}$ and applied to the noise level determined at the first stage:

$$\mu_p \simeq \mu_{p_{10}} Q_{all}. \tag{13}$$

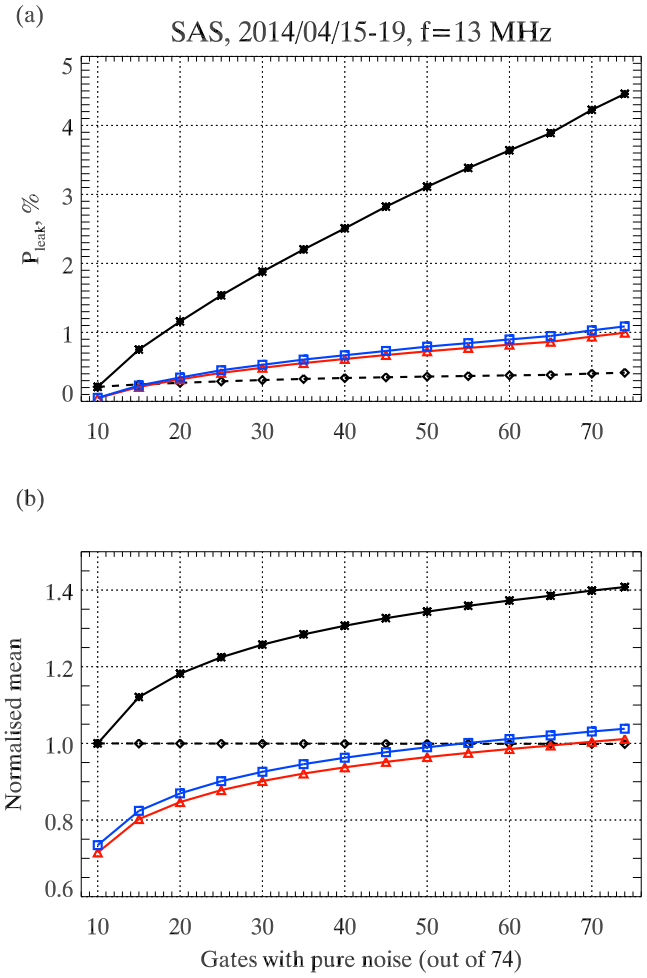

Figure 6. Dependence of the 'leakage' percentage P_{leak} (a) and the normalized mean (b) on the number of range gates with pure noise after applying the maximum possible correction factor Q_{all} (13MHz, SAS, 15–19 April, 2014). The dashed black line corresponds to the noise data obtained from all range gates, the solid black line shows estimates obtained from the ten range gates containing the lowest lag zero power values, and the blue and red lines represent the same ten-gate estimates after applying correction factors based on Chi-Square and Gaussian models, respectively.

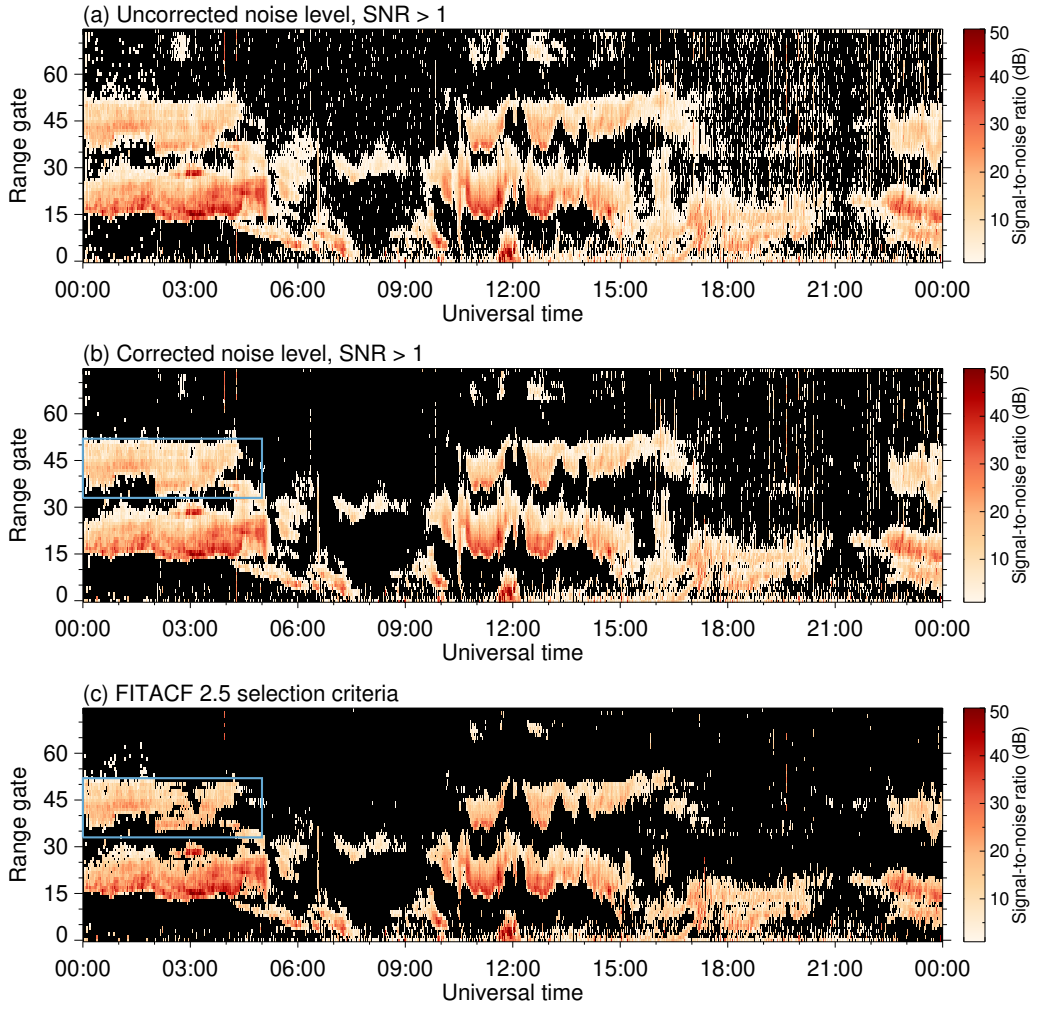

Figure 7. Data pre-selection results for the INV radar on 4 April 2018. The color scale shows the SNR calculated from the lag zero power values shown in Figure 1 and the estimated noise level. (a) Data with SNR>1 determined from the uncorrected noise level. (b) Data with SNR>1 determined from the corrected noise level. (c) Data that satisfy the empirical pre-selection criteria in FITACF2.5 (without the noise level correction). Black shading indicates range gates that do not meet the criteria.

To visualize the effect of the correction procedure on the proposed data pre-selection criterion (SNR>1, equation 4), in Figure 7 we show SNR values calculated for the raw INV dataset that was shown in Figure 1. In the first two panels of Figure 7 we applied the SNR>1 criterion using (a) the uncorrected noise level $\mu_{p_{10}}$, and (b) the corrected noise level $\mu_{p_{10}} Q_{all}$. The range-time cells with rejected data are shaded black. The key difference between these two panels is the amount of low-SNR data points that are isolated in range and time, which are commonly associated with noise. In panel (a) they are highly visible throughout the whole interval, reflecting the excessive noise 'leakage' due to the noise level underestimate. In contrast, the application of the noise level correction (13) drastically decreases the amount of these 'salt and pepper' data in panel (b).

As we mentioned before, the standard FITACF2.5 package applies a complex set of empirical filtering criteria to remove most of these noise-dominated data (Ponomarenko & Waters, 2006). We show the results of applying these criteria (without the noise level correction) in panel (c) of Figure 7. Prior to about 15:00 UT, both the FITACF2.5 criteria (Figure 7c) and the SNR>1 criterion applied to the data with the corrected noise level (Figure 7b) result in a similar amount of noise 'leakage'. However, the spatial extent of areas with the backscatter is noticeably smaller in Figure 7c as FITACF2.5 tends to 'over-filter' physically meaningful low-power data. This can be seen by comparing the amount of backscatter in the regions outlined by the blue rectangles in panels (b) and (c), for example (a 35% difference in this particular case). These results indicate that the combination of the proposed statistically-justified noise correction procedure (13) and the simple SNR threshold for data pre-selection (4) can replace the empirical criteria used by FITACF2.5 for filtering out the data dominated by the atmospheric noise while retaining a larger amount of the valid data.

After 15:00 UT, high-power, short-duration 'streaks' that extend over multiple range gates start to appear in Figure 7. The 'streaks' most likely represent short-duration interference from external HF transmitters, and FITACF2.5 criteria are apparently more effective in removing these signals. However, it is necessary to keep in mind that they also have a detrimental effect on the backscatter returns collected during the same integration time. A simple removal of the affected data in the noise-dominated range gates effectively masks this problem thus preventing its actual resolution. This issue and possible ways to address it will be discussed in more detail in Subsection 4.4.

4 Radar operation and interference effects

So far we have presented datasets where the noise distributions are approximately Gaussian with standard deviation proportional to $1/\sqrt{N_a}$. For these datasets, the proposed noise level correction closely reproduces the actual noise distribution. However, it is important to recognize that the design of SuperDARN operational modes, as well as site-specific technical issues, can significantly alter the noise distribution shape and therefore affect the accuracy of the noise level estimate. In this section we focus on typical operational and technical factors that affect the noise level estimate across substantial portions of the historical SuperDARN dataset.

4.1 Number of averages

One of the important assumptions underlying the noise estimate is that the noise power PDF is Gaussian-shaped with standard deviation $\propto 1/\sqrt{N_a}$. This assumption holds for $N_a \gtrsim 20$ and, therefore, works for the majority of SuperDARN data with a typical $N_a \geq 30$. However, this is not always the case.

In the first decade of SuperDARN operations, the radars normally operated with a two-minute scan duration, providing integration periods of approximately 7 s per beam and $N_a \simeq 70$. However, around 2007 the standard scan duration was reduced to one minute to improve the sampling rate of the data products. The integration period has therefore been reduced to about 3.5 s for a 16-beam radar with only $N_a \simeq 30$–35 pulse sequences available for averaging into a single ACF. Moreover, some radars are currently operating with up to 24 beams, further reducing the number of averages to $\lesssim$25. The model calculations in Figure 4 show that reducing N_a should result in a wider noise PDF with a longer high-power 'tail'.

In Figure 8 we show that this indeed happens to the actual data. The figure shows experimental noise distributions for five different radars with N_a ranging from 10 to 53. Each time interval shown in the Figure was identified by visually selecting range-time intervals with no discernible contribution from backscatter echoes, which is the same method used to produce experimental PDFs in Figure 3. In all five cases we excluded the data in the first 10 range gates and also the last 6 range gates to avoid the effects of meteor scatter and hardware artifacts respectively. These data generally support the theoretical predictions from Figure 4. For $N_a \gtrsim$20, the shapes of the noise histograms are ap-

proximately Gaussian, and, as expected, the width of the distribution increases and a high-power 'tail' becomes more pronounced with decreasing N_a. For the Goose Bay (GBR) and Wallops Island (WAL) data shown by the blue ($N_a = 17$) and dark blue ($N_a = 10$) lines respectively, this 'tail' extends well beyond the SNR=1 threshold, which contaminates the radar data products and reduces the accuracy of the noise level estimation. This issue can be addressed by replacing the Gaussian model approximation with the χ^2 distribution when $N_a \lesssim 20$. However, one needs to be cautious in doing this as, for example, the observed GBR and WAL distributions in Figure 8 are also noticeably wider than their theoretical counterparts (not shown), hinting that some other factors may be affecting the noise statistics for these radars. A potential cause of the observed discrepancy may be related to the fact that during the analyzed time intervals, these two radars were transmitting a customized pulse sequence called 'tauscan'. It was designed to recover receiver samples that cannot be measured using the standard pulse sequences because they coincide with pulse transmissions (Greenwald et al., 2008). The sampling cycle for 'tauscan' takes approximately 200 ms, which is twice as long as the default one, so fewer sequences can be averaged together in the integration period. Importantly, the 'tauscan' ACFs are formed using median rather than mean, and the former produces a significantly higher standard deviation than the latter (e.g., Example 7 on page 257 in Mood, 1963).

4.2 Group range span

Another aspect of radar control program design that may affect the noise level determination is the number and the spatial extent of the range gates, which together determine the group range span sampled by the radar. In the top panel of Figure 9 we show lag zero power measurements by the Bruny Island SuperDARN radar from 1–2 January 2009. During the first twelve hours of this time period, the radar was sampling 70 range gates with a relatively high line-of-sight spatial resolution of 15 km. This setup restricts the total group range sampled by the radar to just over 1000 km, rather than to the standard span of ∼3000–4000 km. During the first few hours in this mode, the radar detected backscatter in almost all of the range gates. As a result, the ten lowest lag zero power values are not representative of the noise level, so the noise power is significantly overestimated. This is evident in the lower panel of Figure 9, which shows that the noise power increases whenever the high-power returns fill most of the FoV (red braces). The over-

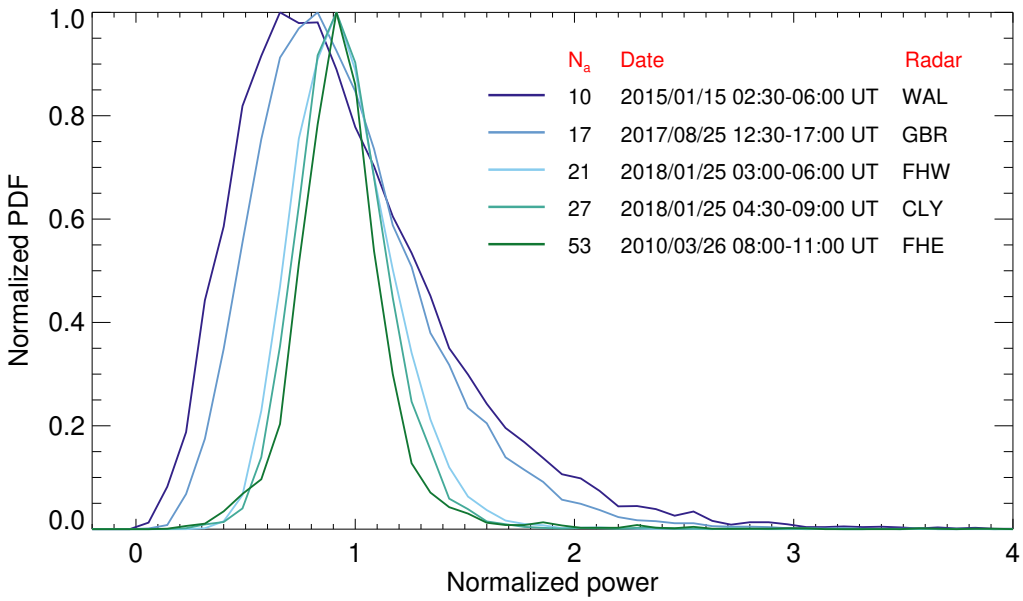

Figure 8. Probability density functions for different numbers of averages N_a, determined from time periods where the radars detected no discernible backscatter in any range gate (beam 7 only).

estimation of the noise power during this experiment would cause a number of ACFs containing coherent backscatter to be rejected as noise.

At 00:00 UT, the radar switches to the standard 45-km range resolution with the same number of range gates, and the noise power shows a sharp decrease. This occurs because the relative number of range gates dominated by noise significantly increases at far ranges so that the noise level is now estimated correctly. These results demonstrate the importance of sampling over a large enough group range span to obtain more than 10 range gates containing noise only. It is apparent from Figure 9 that the range extent of backscatter returns can be 1500 km or more. Therefore, high spatial resolution modes should be designed to sample a proportionally larger number of range gates. The potential range extent of the physically-meaningful backscatter returns should also be considered when selecting radar operating frequencies, since a combination of the multi-hop ionospheric and ground scatter may cover almost the entire FoV at relatively low operating frequencies (i.e., near 10 MHz).

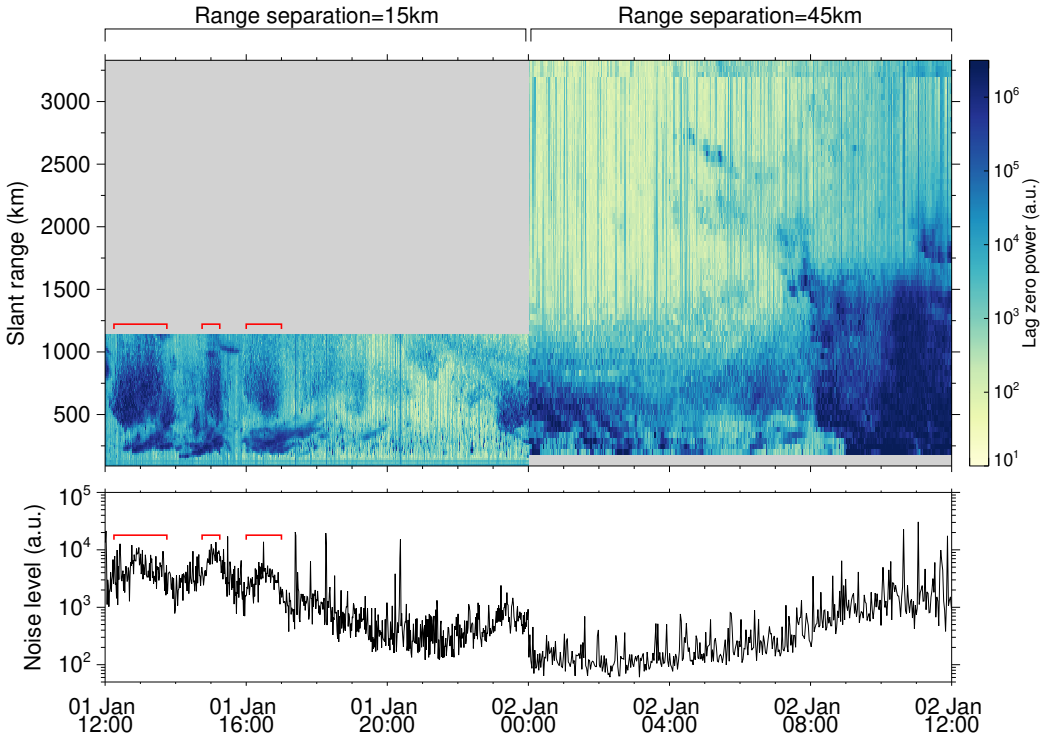

Figure 9. (Top panel) Lag zero power measurements from beam 7 of the Bruny Island SuperDARN radar from 1–2 January 2009. The range gate separation is 15km for the first 12 hours and 45km thereafter, with no change to the total number of range gates. (Bottom panel) Uncorrected noise measurements calculated from the ten lowest values of the lag zero power.

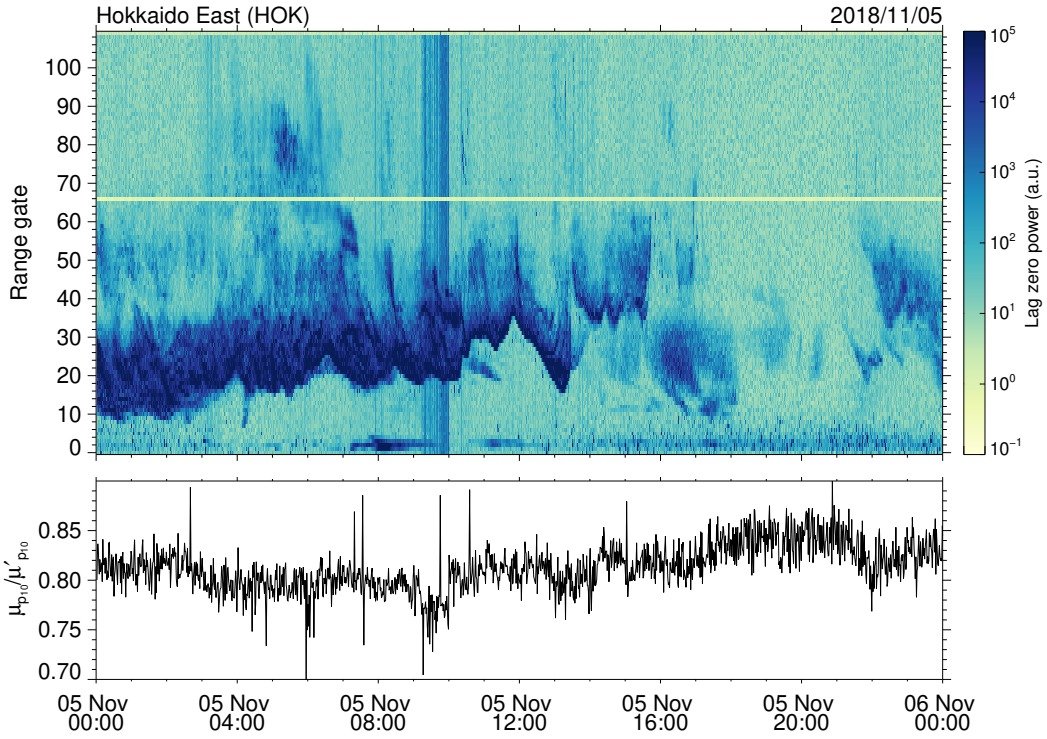

Figure 10. (Top panel) Range-time-intensity plot showing lag zero power measurements from beam 7 of the Hokkaido East radar on 5 November 2018. (Bottom panel) noise underestimation due to the blanked lag zero power values in range gates 66 and 109. $\mu_{p_{10}}$ is the noise calculated using the ten lowest lag zero power measurements (including gates 66 and 109), and $\mu'_{p_{10}}$ is calculated the same way but with gates 66 and 109 excluded.

4.3 Transmitter pulse overlap

SuperDARN radars use the same antennas for transmission and reception of radio signals. This means that samples from the receiver that coincide with pulse transmissions contain no useful information because the receiver channels are 'blanked' to prevent damage to the receiver electronics from the transmitted signals. All FITACF versions account for this 'blanking' procedure by excluding ACF time lags formed using receiver samples measured during a pulse transmission. While this rejection reduces the number of analyzed data, the required echo characteristics such as line-of-sight velocity or spectral width can still be retrieved by fitting model functions to the remaining non-zero lags. In contrast, the lag zero power requires special treatment in the radar operating software to ensure that reliable estimates can be obtained in all range gates. The lag zero power is normally calculated using the samples recorded between the first two pulses in the multi-pulse sequence. The first two pulses are separated by a large enough time delay to sample almost all of the range gates. Beyond the respective maximum range, $R_{\max}$, however, some range gates will also be affected by the 'blanking' procedure and hence contain unphysical lag zero power values. To mitigate this effect, for ranges further than $R_{\max}$, the software utilizes an alternative value of the lag zero power measured using the samples recorded after the last pulse in the sequence, rather than after the first pulse. The value of $R_{\max}$ depends on the pulse sequence design, specifically the time lag to the first range gate and the time lag between the first and second pulses. For the standard SuperDARN pulse sequences, this substitution starts at range gates $R_{\max} = 66$ (8-pulse sequence) or 68 (7-pulse sequence). However, we have identified several instances when this substitution has not been correctly performed, which introduces systematic errors into the noise level estimate.

To illustrate this effect, we show a range-time plot of the lag zero power from the Hokkaido East (HOK) radar in the top panel of Figure 10. In this example, the lag zero power values in range gates 66 and 109 are more than an order of magnitude below the nominal noise level of about 10 a.u.. This indicates that the radar receiver was blanked when the lag zero power was measured in these range gates but the alternative lag zero powers were not used. Since the lag zero power values calculated from the blanked receiver samples are significantly below the nominal noise level, they are always among the ten lowest lag zero power values used for determining the noise level. In the lower panel of Figure 10 we have plotted the ratio $\mu_{p_{10}}/\mu'_{p_{10}}$, where $\mu_{p_{10}}$ is the mean of the ten weak-

est lag zero power values, and $\mu'_{p_{10}}$ is determined using the same method with gates 66 and 109 excluded. We see that the inclusion of gates 66 and 109 in the noise level calculation results in its ∼15–20% underestimation. Since the alternative lag zero power substitution is performed on-site by the radar operating software, the correct lag zero power measurements for gates 66 and 109 cannot be recovered in post-processing. In principle, this issue could be resolved by reprocessing the raw in-phase and quadrature (I&Q) samples, but for most SuperDARN radars these data are not currently recorded.

4.4 Short-duration radio interference

Before each integration period, most SuperDARN radars sample the radio spectrum within a ∼100–500 kHz-wide band around a nominal operating frequency to identify a sub-band that is least affected by noise or interference. While this *'clear' frequency search* is effective at avoiding persistent interference from HF radio transmitters that use continuous wave modes, it is ineffective at avoiding short-duration radio emissions due to the relatively short sampling time of 30-50 ms. Examples of this type of interference are shown in the top panel of Figure 11, where it can be identified as the high-power vertical 'streaks' in the time-range domain. In this plot we also overlay the uncorrected noise $\mu_{p_{10}}$ shown by the white line (right axis). Most of the 'streaks' are accompanied by an increase in the noise level, indicating that the interference affects the lag zero power at all ranges.

In the lower three panels of Figure 11 we show stackplots of the power, phase and frequency shift calculated from the receiver I&Q samples for the first ten pulse sequences in the integration period associated with the 'streak' detected at 08:47:43 UT (indicated by the black arrow in the top panel). This 'streak' is accompanied by a noticeable increase in the noise level. The interference consists of several waveforms characterized by a parabolic phase variation (center panel) and hence a linear frequency progression (right panel) which dominate the received samples in sequences 4–7. The lag zero power 'streak' in the top panel of Figure 11 arises from the I&Q power enhancement during the first 20 ms of sequence 6 (left panel).

The effect of the short-duration interference could potentially be mitigated earlier in the data processing workflow by replacing the mean with the median when averaging ACF lags, since the median is much less sensitive to outliers. However, one has to

be cautious with applying the median to data unaffected by interference as it results in a significantly higher standard deviation than the mean (see the end of Subsection 4.1).

5 Summary and conclusions

In this study we have shown that the standard SuperDARN data analysis software (FITACF2.5) systematically underestimates the noise level by up to 40%. This underestimation occurs because the software determines the noise level using only the low-power tail of the total noise distribution, and results in a significant increase in the amount of the noise data being misidentified as valid backscatter echoes. This contamination may impact the quality of the higher-level SuperDARN data products. For example, it has been shown that SuperDARN global plasma circulation ('convection') maps can be significantly distorted by velocity measurements that did not originate from the ionospheric F region backscatter (Chisham & Pinnock, 2002; Ponomarenko et al., 2008). The same is applicable to the noise-dominated data discussed here.

We propose a procedure that provides an accurate estimate of the noise level by correcting the standard FITACF2.5 estimate using predicted noise statistics derived from the number of sampled range gates N_{g} and the number of averages N_a. Based on theoretical and observational data, we assume that the noise power is characterised by a Gaussian PDF with standard deviation $\propto 1/\sqrt{N_a}$. This correction procedure has been validated using noise data from several SuperDARN radars operating at frequencies between 10.3 and 13.3 MHz. Furthermore, the more accurate noise estimates allowed us to propose and to validate a simple data pre-selection criterion that can replace the empirical procedures used in FITACF2.5. However, it is important to emphasize that the proposed threshold of SNR=1 is arbitrary, and it may be appropriate to raise or lower its value to suit the intended science application and/or the desired level of statistical significance. For example, one could consider using an N_a-dependent SNR threshold that restricts the 'leaked' noise percentage to a pre-determined level.

We have also identified other factors that impact the accuracy of the noise level determination that are related to the radar software, control program design and external radio interference, and have discussed ways to resolve these issues. Some effects, like those caused by the missing alternative lag zero power values, can be resolved by a simple exclusion of the affected range gates. However mitigating other effects might require a more

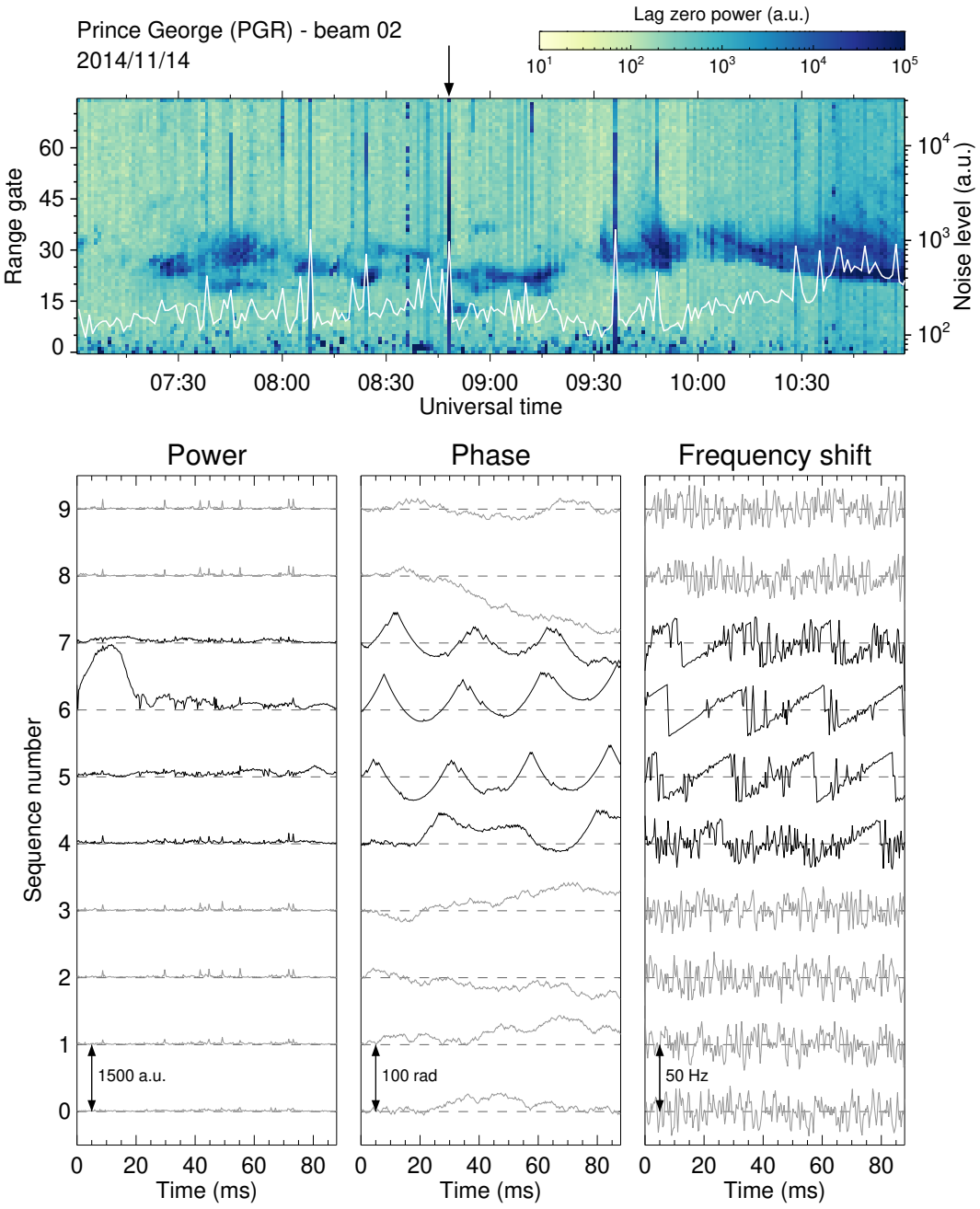

Figure 11. The top panel shows a time-range map for the raw lag zero power measurements from beam 2 of the Prince George radar from 07:00–11:00 UT on 14 November 2014. The overlaid solid white line shows the uncorrected noise measurements with scale shown on the right axis. The three panels below are stackplots of the power, phase and frequency shift for the first ten transmit-receive cycles associated with the lag zero power 'streak' indicated by the arrow at 08:47:43 UT.

in-depth approach. For example, short-lived external interference can only be removed from the averaged ACF by re-processing the I&Q samples, and as the I&Q data are not recorded for the majority of the radars, a larger portion of the current SuperDARN dataset affected by these issues cannot readily be corrected by post-processing. The same can be said about ACFs with a low number of averages and about other situations when the noise PDF shape significantly differs from Gaussian. However, in this case the 'leaked' noise/interference manifests itself as isolated pixels in the time-range domain, so most of this 'salt-and-pepper' contamination can be effectively removed by additional filtering based, e.g, on the number of valid returns ('good neighbours') in the surrounding time-range cells. It is important to recognize that impacts from these factors are site-specific, so the level of the noise contamination may vary significantly between radars. This presents challenges when combining data from multiple radars into a single data product (e.g., in plasma circulation mapping). Furthermore, applying a consistent SNR threshold for all radars is especially important in studies that compare backscatter occurrence between different radars (e.g. Ghezelbash et al., 2014), since the SNR is frequently used to select valid backscatter data.

6 Open research

Raw SuperDARN data used in this study together with the licensing information and data description are available from Federated Research Data Repository (FRDR), Canada, at (Super Dual Auroral Radar Network, 2021a, 2021b, 2021c, 2021d, 2021e, 2021f). The RAWACF data can be read using the Radar Software Toolkit (RST) written in C (SuperDARN Data Analysis Working Group, 2021).

Acknowledgments

PP is supported by GO Canada Grant G00024607 from the Canadian Space Agency. The work of EB was supported by a grant from the Canada Foundation for Innovation, and also by the Japan Society for the Promotion of Science (JSPS): Project Number: 16H06286. The work of NN was supported by Japan Society for the Promotion of Science (JSPS): Project Numbers: 16H06286, 18KK0099, 19K03949, 21H04518. The authors acknowledge the use of SuperDARN data. SuperDARN is a collection of radars funded by the national scientific funding agencies of Australia, Canada, China, France, Italy, Japan, Norway, South Africa, United Kingdom and United States of America. The authors thank

K. Sterne (Virginia Tech) and M. Schmidt (University of Saskatchewan) for helpful discussions and assistance with data access.

References

André, D., Sofko, G., Baker, K., & MacDougall, J. (1998). Superdarn interferometry: Meteor echoes and electron densities from groundscatter. *J. Geophys. Res.*, *103(A4)*, 7003-7015. doi: 10.1029/97JA02923

Baker, K. B., Greenwald, R. A., Villain, J.-P., & Wing, S. (1988). *Spectral characteristics of high frequency (HF) backscatter for high latitude ionospheric irregularities: Preliminary analysis of statistical properties* (Tech. Rep.). Rome Air Development Center, Griffiss Air Force Base, Rome, NY: John Hopkins University.

Barthes, L., André, R., Cerisier, J.-C., & Villain, J.-P. (1998). Separation of multiple echoes using a high-resolution spectral analysis for SuperDARN HF radars. *Radio Sci.*, *33*, 1005-1017. doi: 10.1029/98RS00714

Bendat, J. S., & Piersol, A. G. (2010). *Random data: Analysis and measurement procedures* (4th ed.). John Wiley & Sons, Inc.

Berngardt, O. I. (2020). Noise level forecasts at 8–20 MHz and their use for morphological studies of ionospheric absorption variations at EKB ISTP SB RAS radar. *Advances in Space Research*, *66*(2), 278–291. doi: 10.1016/j.asr.2020.04.005

Berngardt, O. I., Ruohoniemi, J. M., St-Maurice, J.-P., Marchaudon, A., Kosch, M. J., Yukimatu, A. S., ... Lester, M. (2019). Global diagnostics of ionospheric absorption during x-ray solar flares based on 8-to 20-MHz noise measured by over-the-horizon radars. *Space Weather*, *17*(6), 907–924.

Berngardt, O. I., Voronov, A. L., & Grkovich, K. V. (2015). Optimal signals of golomb ruler class for spectral measurements at ekb superdarn radar: Theory and experiment. *Radio Science*, *50*(6), 486-500. Retrieved from `https://agupubs.onlinelibrary.wiley.com/doi/abs/10.1002/2014RS005589` doi: https://doi.org/10.1002/2014RS005589

Bland, E. C., Heino, E., Kosch, M. J., & Partamies, N. (2018). SuperDARN radar-derived HF radio attenuation during the September 2017 solar proton events. *Space Weather*, *16*. doi: 10.1029/2018SW001916

Bland, E. C., Partamies, N., Heino, E., Yukimatu, A. S., & Miyaoka, H. (2019). Energetic electron precipitation occurrence rates determined using the Syowa East SuperDARN radar. *Journal of Geophysical Research: Space Physics*, *124*(7), 6253–6265. doi: 10.1029/2018JA026437

Chakraborty, S., Baker, J. B. H., Ruohoniemi, J. M., Kunduri, B., Nishitani, N., & Shepherd, S. G. (2019). A study of SuperDARN response to co-occurring space weather phenomena. *Space Weather*, *17*(9), 1351–1363. doi: 10.1029/2019SW002179

Chisham, G., Burrell, A. G., Marchaudon, A., Shepherd, S. G., Thomas, E. G., & Ponomarenko, P. (2021). Comparison of interferometer calibration techniques for improved superdarn elevation angles. *Polar Science*, *28*, 100638. Retrieved from `https://www.sciencedirect.com/science/article/pii/S1873965221000025` (SuperDARN / Studies of Geospace Dynamics - Today and Future) doi: https://doi.org/10.1016/j.polar.2021.100638

Chisham, G., Lester, M., Milan, S. E., Freeman, M. P., Bristow, W. A., Grocott, A., ... Walker, A. D. M. (2007). A decade of the Super Dual Auroral Radar Network (SuperDARN): Scientific achievements, new techniques and future directions. *Surv. Geophys.*, *28*, 33–109. doi: 10.1007/s10712-007-9017-8

Chisham, G., & Pinnock, M. (2002). Assessing the contamination of superdarn global convection maps by non-f-region scatter. *Ann. Geophys.*, *20*, 13-28.

Ghezelbash, M., Koustov, A. V., Themens, D. R., & Jayachandran, P. T. (2014). Seasonal and diurnal variations of PolarDARN F region echo occurrence in the polar cap and their causes. *Journal of Geophysical Research: Space Physics*, *119*(12), 10–426.

Greenwald, R. A., Baker, K. B., Dudeney, J. R., Pinnock, M., Jones, T. B., Thomas, E. C., ... Yamagishi, H. (1995). DARN/SuperDARN: A global view of the dynamics of high-latitude convection. *Space Sci. Rev.*, *71*, 761-795.

Greenwald, R. A., Baker, K. B., Hutchins, R. A., & Haniuse, C. (1985). An hf phased-array radar for studying small-scale structure in the high-latitude ionosphere. *Radio Sci.*, *20*, 63–79.

Greenwald, R. A., Oksavik, K., Barnes, R., Ruohoniemi, J. M., Baker, J., & Talaat, E. R. (2008). First radar measurements of ionospheric electric fields at sub-second temporal resolution. *Geophysical Research Letters*, *35*(3). doi:

10.1029/2007GL032164

Hall, G. E., MacDougall, J. W., Moorcroft, D. R., St-Maurice, J.-P., Manson, A. H., & Meek, C. E. (1997). Super Dual Auroral Radar Network observations of meteor echoes. *Journal of Geophysical Research: Space Physics*, *102*(A7), 14603–14614. doi: 10.1029/97JA00517

ITU-R P.372-8. (2019). *Recommendation ITU-R P.372-8*—Radio Noise (Tech. Rep.). International Telecommunications Union (ITU). Retrieved from `https://www.itu.int/rec/R-REC-P.372`

Milan, S. E., Jones, T. B., Robinson, T. R., Thomas, E. C., & Yeoman, T. K. (1997). Interferometric evidence for the observation of ground backscatter originating behind the CUTLASS coherent HF radars. *Annales Geophysicae*, *15*(1), 29–39. doi: 10.1007/s00585-997-0029-y

Mood, A. M. (1963). *Introduction to the theory of statistics.* New York : McGraw-Hill.

Nishitani, N., Ruohoniemi, J. M., Lester, M., Baker, J. B. H., Koustov, A. V., Shepherd, S. G., ... others (2019). Review of the accomplishments of mid-latitude Super Dual Auroral Radar Network (SuperDARN) HF radars. *Progress in Earth and Planetary Science*, *6*(27). doi: 10.1186/s40645-019-0270-5

Ponomarenko, P. V., Iserhienrhien, B., & St-Maurice, J.-P. (2016). Morphology and possible origins of near-range oblique HF backscatter at high and midlatitudes. *Radio Science*, *51*(6), 718–730.

Ponomarenko, P. V., & Waters, C. L. (2006). Spectral width of superdarn echoes: Measurement, use and physical interpretation. *Ann. Geophys.*, *24*, 115–128. doi: 10.5194/24-115-2006

Ponomarenko, P. V., Waters, C. L., & Menk, F. W. (2008). Effects of mixed scatter on SuperDARN convection maps. *Annales Geophysicae*, *26*, 1517–1523. doi: 10.5194/angeo-26-1517-2008

Reimer, A. S., Hussey, G. C., & McWilliams, K. A. (2018). Statistically self-consistent and accurate errors for SuperDARN data. *Radio Science*, *53*(1), 93–111. doi: 10.1002/2017RS006450

Ribeiro, A. J., Ruohoniemi, J. M., Ponomarenko, P. V., Clausen, L. B. N., Baker, J. B. H., Greenwald, R. A., ... de Larquier, S. (2013). A comparison of SuperDARN ACF fitting methods. *Radio Science*, *48*(3), 274–282. doi:

10.1002/rds.20031

Shepherd, S. G. (2017). Elevation angle determination for SuperDARN HF radar layouts. *Radio Science*, *52*(8), 938–950. doi: 10.1002/2017RS006348

Super Dual Auroral Radar Network. (2021a). *SuperDARN 2009 RAWACF* [dataset]. Federated Research Data Repository. https://doi.org/10.20383/102.0453.

Super Dual Auroral Radar Network. (2021b). *SuperDARN 2010 RAWACF* [dataset]. Federated Research Data Repository. https://doi.org/10.20383/102.0448.

Super Dual Auroral Radar Network. (2021c). *SuperDARN 2014 RAWACF* [dataset]. Federated Research Data Repository. https://doi.org/10.20383/102.0452.

Super Dual Auroral Radar Network. (2021d). *SuperDARN 2015 RAWACF* [dataset]. Federated Research Data Repository. https://doi.org/10.20383/102.0447.

Super Dual Auroral Radar Network. (2021e). *SuperDARN 2017 RAWACF* [dataset]. Federated Research Data Repository. https://doi.org/10.20383/101.0289.

Super Dual Auroral Radar Network. (2021f). *SuperDARN 2018 RAWACF* [dataset]. Federated Research Data Repository. https://doi.org/10.20383/101.0290.

SuperDARN Data Analysis Working Group. (2021). *SuperDARN Radar Software Toolkit (version 4.6)* [software]. Zenodo. Retrieved from `https://doi.org/10.5281/zenodo.5156752` (Participating members: Schmidt, M.T., Bland, E.C., Thomas, E.G., Burrell, A.G., Coco, I., Ponomarenko, P.V., Reimer, A.S., Sterne, K.T., and Walach, M.-T.) doi: 10.5281/zenodo.5156752

Villain, J.-P., André, R., Hanuise, C., & Gresillon, D. (1996). Observation of the high-latitude ionosphere by HF radars: Interpretation in terms of collective wave scattering and characterization of the turbulence. *J. Atmos. Sol. Terr. Phys.*, *58*, 943-958. doi: 10.1016/0021-9169(95)00125-5